Polyhedron 210 (2021) 115504

Contents lists available at ScienceDirect

Polyhedron

journal homepage: www.elsevier.com/locate/poly

# Structurally diverse heterobimetallic Pb(II)-Salen complexes mechanistic notion of cytotoxic activity against neuroblastoma cancer cell: Synthesis, characterization, protein–ligand interaction profiler, and intuitions from DFT

Dhrubajyoti Majumdar [a,b], Burak Tüzün [c], Tapan Kumar Pal [d], Reena V. Saini [e,*], Kalipada Bankura [a], Dipankar Mishra [a,*]

[a] Department of Chemistry, Tamralipta Mahavidyalaya, Tamluk 721636, West Bengal, India
[b] Department of Chemistry, Indian Institute of Technology (Indian School of Mines), Dhanbad, Jharkhand 826004, India
[c] Sivas Cumhuriyet University, Sivas Vocational School, Department of Plant and Animal Production, TR-58140 Sivas, Turkey
[d] Department of Chemistry, Pandit Deendayal Petroleum University, Gandhinagar 382007, India
[e] Department of Biotechnology, Maharishi Markandeshwar (Deemed to be University), Mullana-Ambala, Haryana 133207, India

ARTICLE INFO

*Keywords:*
Salen ligands
Heterobimetallic complex
Neuroblastoma cell
Cytotoxicity
DFT

ABSTRACT

In this work, two new heterobimetallic Pb(II) complexes, namely [Zn($L^1$)($\eta^1$-NCS)Pb($\eta^1$-SCN)] **(1)** and [Cd($L^2$)($\eta^1$-NCS)Pb($\eta^1$-SCN)]$_n$ **(2)** integrated from Salen ligands ($L^1$/$L^2$) in the presence of NaSCN. The title compounds were characterized with microanalytical, spectroscopic techniques, and SC-XRD. SC-XRD divulges a deprotonated form of ligands trapped by M(II) ions into the $N_2O_2$ compartment (M = Zn/Cd), whereas more compelling Pb(II) ions outer $O_4$ cavities. The tethering thiocyanate linkers formed the discrete **(1)** and the 1D polymer **(2)**. We accomplished the DFT using B3LYP, HF, and M062X with Lanl2dz level basis sets to delineate Frontier molecular orbital (FMO), the complex biological activity, and the Global chemical parameters. Molecular docking (MD) finds the plausible binding mechanism by implanting the complexes into the active site of crystal systems of the BRCT repeat region from the breast cancer-associated protein, VEGFR kinase liver cancer protein, and an allosteric Eya2 lung cancer protein. Polar and hydrophobic exchanges, π-π interaction, hydrogen bonds, and Bromine are the essential binding process. Protein-Ligand Interaction Profiler (PLIP) examined the interaction of the protein with complex **1**. We consider the mechanistic perception of cytotoxic action, apoptosis cancer cell death via intracellular reactive oxygen species (ROS) generation, and mitochondrial membrane potential (MMP) of apoptotic cells with SH-SY5Y human neuroblastoma cancer cells. The enhanced ROS generation and mitochondrial depolarization in SH-SY5Y cells indicate apoptosis in these cells. We explain the Western blot-activated caspase-3 in lysates of SH-SY5Y cells for the apoptotic pathway, exploring the induction of apoptotic pathways via 1 and 2 in neuroblastoma cells.

## 1. Introduction

Beyond a lingering moment, there has been a precedented boom within the coordination chemistry of the $N_2O_4$ compartmental-type Salen ligand. Such ligands can more easily form polynuclear complexes that follow the simple synthetic method [1], consisting of inner $N_2O_2$ and outer $O_4$ compartments (Scheme S1) [2–7]. These compartments are competent for entrapping versatile metal ions in their $N_2O_2$ and other compelling external $O_4$ enclosures [8-12] (Scheme S2). So far, they have hitherto been used to develop varieties of hetero-nuclear 3d/4f complexes [13]. Such heteronuclear complex applications are magnetism, catalysis, biological experiments, molecular architectures [14a–c], Schottky diode, etc. [15a–d]. The complex networks can employ for the selective transport of ions [16], biomimetic catalysts [17a–c], the activation, storage, and transportation of aerial dioxygen molecules in enzymatic pathways [18]. In the 21st century, cancer is a fatal disorder in developing countries [19a,b,e,20,21]. Rosenberg's triumph of cisplatin discovery in 1965 and related platinum-based drugs as

* Corresponding authors.
*E-mail addresses:* reenavohra10@gmail.com (R.V. Saini), dmishra.ic@gmail.com (D. Mishra).

https://doi.org/10.1016/j.poly.2021.115504
Received 21 June 2021; Accepted 24 September 2021
Available online 2 October 2021

anticancer agents [22] reinforced the scientists to realize more scrupulous and fewer metallopharmaceuticals [22]. The investigations are based on the observations that using cisplatin in curative therapy is associated with severe clinical problems [22]. In addition, the therapeutic application of metallic complexes remains an unexplored area of research. Cancer researchers now recognize that the prosperity of cancer biology knowledge has led to phenomenal cancer prevention. Neuroblastoma is an innovative, sympathetic nervous system that almost only occurs in early childhood (90% of cases are diagnosed by age 5). One cancer form in nerve cells called neuroblasts (immature nerve tissue) is a leading cause of pediatric cancer death for children between 1 and 5. It accounts for 12%–15% of all pediatric cancer-related mortality [23a–d]. Diagnosed two years can lead to many clinical outcomes, from spontaneous tumour regression to metastatic disorder with poor prognosis [24]. It is noteworthy that the coordination chemistry of Pb(II) is not 'untouchable.' The new synthesis of Ni(II)/Pb(II) coordination polymer motivates our researchers to search for novel Pb(II) Salen complexes. The binding thiocyanate linkers added to the Zn/Cd/Pb metal ions influence the discrete/polymeric complex formation (Scheme S4) [16]. The high atomic number (Z = 82), large radius, adequate to embrace other coordination numbers from 2 to 10 to continue in variable valence states, and skillful coordination chemistry attracted synthetic inorganic chemists to map unique lead complexes [25–28]. Lead is lethal [16] and must embrace good safe gourds to synthesize its complexes. Lead materials are trained in semiconductors, batteries, ferroelectric, and nonlinear optical [29–33]. In addition, two distinct structural organizations characterize the Lead Tetrel bonds [34]. The electronic configuration [Xe]$4f^{14}5d^{10}6s^{2}6p^{2}$ makes inadequate screening of $4f^{14}$ and $3d^{10}$ electrons produce the 6 $s^{2}$ electron pair inert. The high penetrating property of the 6s orbital and the relativistic stabilization of $6s^{2}$ electrons are too rational for the inert pair effect [35–39]. However, this lone pair is stereo-dynamic and inactive in few complexes, attending to Hemi-directional [39,40] or driving to Holo-directed complexes (Scheme S3) [41]. Meanwhile, Zn/Cd complex ground states have no significance CFSE, primordial for other $d^{n}$ electronic systems (n = number of d orbital electrons) [42a,b,43a–c]. Zn is the 2nd most crucial abundant metal ion in the human body after Fe, payable to its intense engagement in several biochemical functions [44,45] or complexes [46a–f,47,48a,b]. The DFT, MD, and PLIP experiments enchant the coordination chemistry to combine the experimental and theoretical biological activities [49a–c].

In this endeavour, we presented for the synthesis, spectroscopic characterization, X-ray crystal structures, PLIP, and DFT of two novels lead complexes, [Zn($L^{1}$)(η1-NCS)Pb(η1-SCN)] (1) and [Cd($L^{2}$)(η1-NCS)Pb(η1-SCN)]n (2). Herein, the significant SH-SY5Y human neuroblastoma cancer cell line mechanistic effect accomplishes on the Lead complexes.

## 2. Experimental section

### 2.1. Starting materials and instrumentation

All research chemicals and solvents were of reagent grade, used as purchased with no further purification. $Zn(OAc)_2{\cdot}2H_2O$, $Cd(OAc)_2{\cdot}2H_2O$, $Pb(NO_3)_2$, Sodium thiocyanate (NaSCN), 5-Bromo-3-methoxy-2-hydroxybenzaldehyde, 3-ethoxy-2-hydroxybenzaldehyde, 1,3-diaminopropane, and 2,2-dimethyl-1,3-propanediamine were bought from the Sigma Aldrich Company, USA. Elemental (CHN) was completed on a PerkinElmer 2400 elemental analyzer. FT-IR and Raman spectra of solid samples were recorded as KBr pellets (4000–400 $cm^{-1}$) using a Perkin–Elmer spectrum RX 1 and BRUKER RFS 27 (4000–50 $cm^{-1}$) model. $^{1}H$ and $^{13}C$ NMR spectra were collected on a Bruker 400 MHz and 75.45 MHz FT-NMR spectrometer operating tetramethylsilane (TMS) as an internal standard in DMSO-$d_6$. Energy-dispersive X-ray spectroscopy (EDX) experiments were carried out on EDX OXFORD XMX N using Tungsten filament. BRUKER AXS performed powder X-ray diffraction (PXRD) measurements and the GERMANY X-ray diffractometer D8 FOCUS model using Cu Kα-1 radiation. UV–Visible spectra in $CH_3OH$ (Salen ligands) and DMSO (complexes) (200–1100 nm) were determined using the Hitachi model U-3501 spectrophotometer.

### 2.2. DFT methodology

DFT methods have been analyzed by the chemical and biological activities of the Salen complexes using a Gaussian software program (B3LYP, HF, and M062X with Lanl2dz level basis sets) [50]. DFT calculated various parameters such as EHOMO, ELUMO, ΔE energy gap (ΔE = EHOMO-ELUMO), chemical hardness (η), chemical potential (μ), nucleophilicity (ε), electronegativity (χ), electrophilicity (ω), and global softness (σ) provided valuable information about the examined metal complexes. We compared the biological activities of the molecules against cancer proteins. The popular HEX 8.0.0 programs reviewed the proteins and metal complexes files [51]. Molecular docking experiments used the crystal structure of the BRCT repeat region from the breast cancer-associated protein, crystal structure of VEGFR kinase (liver cancer) protein, and crystal structure of an allosteric Eya2 phosphatase inhibitor (lung cancer) protein. We used the following parameters for docking: correlation type shape only, FFT mode: 3D, grid dimension: 0.6, receptor range: 180, ligand range: 180, twist range: 360, distance range: 40. Last, the Protein-Ligand Interaction Profiler (PLIP) server examined protein and the metal complex's interactions [52a–d].

### 2.3. Methodology of cancer cells

#### 2.3.1. Cell culturing and maintenance

SH-SY5Y (Human neuroblastoma cell line) cells were procured from National Centre for Cell Sciences (NCCS), Pune, India. The stock cells were cultured in tissue culture flasks with DMEM/Ham's F-12 (1:1) media, complemented by 10% inactivated fetal bovine serum (FBS), 1% penicillin–streptomycin in a humidified atmosphere of 5% $CO_2$ at 37 °C up to 80–90% confluent. Used media was removed, followed by phosphate-buffered saline (PBS) wash to remove the dead cells and debris. Trypsinization of cells was carried out using 0.25% of trypsin solution. Further centrifugation was done at 2000 rpm for 10 min. The pellet was then cultivated and transferred to new cultural dishes for subculturing.

#### 2.3.2. In vitro cytotoxicity

The cytotoxic effects of the Salen ligands, free metal salts and the complexes were determined by MTT (3-(4,5-dimethylthiazol-2-yl)-2,5-diphenyl tetrazolium bromide) assay [52a–d]. The cells like SH-SY5Y were seeded at a density of 1 × $10^{4}$ cells/ mL in a 96-well plate, incubated for 24 h (37 °C, 5% $CO_2$). The next day, compounds were treated (5–40 μM) for 24 h followed by 4 h incubation with MTT. Paclitaxel and DMSO were used as positive and vehicle controls. After 4 h incubation, 100 μl of DMSO was added into each well for dissolving the purple-colored complex. The optical density was noted at 595 nm using a microplate reader. $IC_{50}$ values of the compounds were reported as an average of three replicates. Cell death was analyzed employing the following formula:

$$\%\ Cell\ death\ =\ \left(Abs_{control} - -Abs_{sample}\right)/Abs_{control}X\ 100$$

#### 2.3.3. Intracellular reactive oxygen species (ROS) generation

SH-SY5Y cells (1 × $10^{5}$ cells/well) were cultured in six-well plates and incubated for 24 h. First, the cells were treated with C1 & C2 (10 μM) for 4 h. Next, the cells were washed with PBS and incubated with $H_2$DCF-DA (2′,7′-dichlorodihydrofluorescein diacetate) probe at a final concentration of 20 μM at 37 °C for 20 min. Then, the stained cells were washed twice and resuspended in PBS·$H_2O_2$ (100 μM) treated cells act as a positive control, and untreated cells were used as a negative control. The fluorescence was detected using a microplate reader (Spectramax

**Table 1**
Crystal data and structure refinement parameters.

| Formula | $C_{21}H_{18}Br_2N_4O_4PbS_2Zn$ (**1**) | $C_{25}H_{28}CdN_4O_4PbS_2$ (**2**) |
|---|---|---|
| M/g | 886.89 | 832.22 |
| Crystal system | Monoclinic | Orthorhombic |
| Space group | *P 1 21/n 1* | P 21 21 21 |
| *a*/Å | 7.8371(5) | 9.4389(7) |
| *b*/Å | 9.2809(5) | 16.2885(13) |
| *c*/Å | 35.6227(19) | 18.7829(14) |
| *β* (°) | 94.901(2) | 90 |
| *V*/Å$^3$ | 2581.6(3) | 2887.8(4) |
| *Z* | 4 | 4 |
| $\rho_c$/gcm$^{-3}$ | 2.282 | 1.914 |
| $\mu$/mm$^{-1}$ | 10.735 | 6.740 |
| *F* (000) | 1672 | 1600.0 |
| Cryst size (mm$^3$) | 0.045 × 0.031 × 0.021 | 0.26 × 0.24 × 0.20 |
| *θ* range (deg) | 2.477 to 28.466 | 2.415 to 27.560 |
| Limiting indices | $-10 \le h \le 10$<br>$-12 \le k \le 12$<br>$-47 \le l \le 47$ | $-11 \le h \le 12$<br>$-14 \le k \le 21$<br>$-24 \le l \le 22$ |
| Reflns collected | 52,652 | 24,325 |
| Ind reflns | 6508 [$R_{int}$ = 0.0628, *R*sigma = 0.0349] | 6684 [$R_{int}$ = 0.0499, $R_{sigma}$ = 0.0457] |
| Completeness to *θ* (%) | 0.999 | 0.999 |
| Refinement method | Full-matrix-block least-squares on F$^2$ | Full-matrix-block least-squares on F$^2$ |
| Data/restraints/ parameters | 6508/0/318 | 6684/0/338 |
| Goodness-of-fit on $F^2$ | 1.078 | 1.055 |
| Final *R* indices [$I > 2\sigma(I)$] | $R_1$ = 0.0372<br>w$R_2$ = 0.0831 | $R_1$ = 0.0415<br>w$R_2$ = 0.0887 |
| R indices (all data) | $R_1$ = 0.0493<br>w$R_2$ = 0.0877 | $R_1$ = 0.0547<br>w$R_2$ = 0.0965 |
| Largest diff. peak and hole (e·Å$^{-3}$) | 1.314 and −1.236 | 1.582 and −0.966 |

ID3 microplate reader, Molecular Devices, USA). The excitation and emission wavelengths were recorded at 485 nm and 538 nm [52a–d]. The results were expressed as a fold increase in ROS production compared to the untreated cells.

### 2.3.4. Mitochondrial membrane potential (MMP)

SH-SY5Y cells (1 × 10$^5$ cells/well) were seeded in six-well plates to analyze the mitochondrial membrane potential and could grow for 24 h. The next day, cells were treated for 4 h with C1 & C2 (10 μM). After washing with PBS, cells were incubated with Rhodamine 123 (20 μM) for 20 min at 37 °C. In the meantime, the cells were washed twice with PBS, followed by fluorescence measurement at an excitation wavelength of 511 nm. An emission wavelength of 534 nm [52a–d] and the results were expressed as relative fluorescence units. Paclitaxel (1 μM) was used as a positive control and cells in PBS without stain as blank control.

### 2.3.5. Morphology of apoptotic cells

SH-SY5Y cells were cultured (5 × 10$^4$ cells/well) and treated with 10 μM of C1 & *C*2 for 24 h. Paclitaxel (1 μM) was used as a positive control. The cells were washed twice with PBS and fixed in 4% paraformaldehyde for 10 min. After washing with PBS, cells were permeabilized with 0.1% Triton-X 100 for 10 min followed by Hoechst-33342 (1 μg/ml) staining for 20 min in the dark. Therefore, washing three times with PBS was carried out, and the nuclear morphology of cells imaged was under a fluorescent microscope (Carl Zeiss Microscopy, Germany) at 20 × magnification.

### 2.3.6. Western blot analysis

SH-SY5Y (5 × 10$^5$ cells/well) were cultured in six-well plates and treated with C1 & *C*2 (10 μM), Paclitaxel (1 μM) for 24 h. The cells were harvested and washed twice with ice-cold PBS. Then lysed with a hypotonic buffer with 10 mM Tris–HCl (pH 8.0) and 1 mM EDTA (Ethylenediaminetetraacetic acid) by freeze–thaw cycles. Therefore, the cell lysates were electrophoresed on 12% SDS-PAGE and transferred to the nitrocellulose membrane. First, blocking was done for 1 h using 5% skimmed milk at room temperature. Then, the membranes were subjected to primary antibodies directed against caspase-3 (BioLegend) and beta-actin (1:1000) overnight at 4 °C in PBS with 0.1% Tween-20 (PBST). Then, membranes were incubated for 1 h at room temperature with an anti-mouse horseradish peroxidase-conjugated secondary antibody at a dilution of 1:3000. Protein bands were detected using enhanced chemiluminescence (ECL kit, Advansta) using Chemidoc (FluorChem M, Bio-techne, USA).

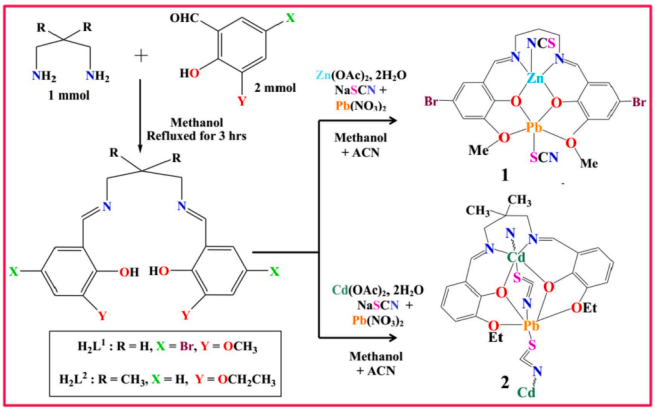


**Scheme 1.** Synthetic Strategy for Salen ligands and the heteronuclear complexes.

### 2.4. Crystallographic data collection and refinement

Crystals were grown after slow evaporation of the methanol solvent in the presence of a few drops of ACN (acetonitrile). After the right choice of good quality 3–4 crystals (under microscopic observance), crystal data have been collected on a Bruker CCD [53] diffractometer using Mo $K_\alpha$ radiation at λ = 0.71073 Å. Herein we have used a few famous crystallographic programs: *SMART* used for accumulating frames of information, indexing reflections, and determining lattice parameters, *SAINT* [54] for the combination of the intensity of reflections, and scaling, *SADAB* [55] for absorption correction, and *SHELXTL* for space group, structure determination and least-squares refinements on $F^2$. The crystal structure was solved utilizing full-matrix least-squares techniques against $F^2$ using *SHELXL*-2014 [56] and *Olex-2* software [57]. All the non-H atoms had been refined with anisotropic displacement parameters, and all hydrogen positions were constant at calculated positions, which can be delicate isotropically. The complete crystallographic information and structure refinement parameters are presented in Table 1.

### 2.5. Synthesis of N,N′-bis(5-bromo-3-methoxysalicylidenimino)-1,3-diaminopropane ($H_2L^1$) and N,N′-bis(3-ethoxysalicylidene)-2,2-dimethyl-1,3-propanediamine ($H_2L^2$)

Two Salen ligands have been synthesized following the literature method (Scheme1) [42a]. The reflux condensation of 5-Bromo-3-methoxy-2-hydroxybenzaldehyde (0.231 g, 1 mmol) with 1,3-diaminopropane (0.0371 g, 0.5 mmol) in (50 mL) methanol at 80 °C for 3hr prepared $H_2L^1$. An identical procedure was used to synthesize $H_2L^2$ except 2,2-dimethyl-1,3-propanediamine (0.0511 g, 0.5 mmol) condensed with 3-ethoxy-2-hydroxybenzaldehyde (0.166 g, 1 mmol). Finally, the solvent was removed under vacuum and the yellow powder product separated upon cooling, the solution collected and air-dried. N, N′-bis(5-bromo-3-methoxysalicylidenimino)-1,3-diaminopropane ($H_2L^1$): Yield: 0.215 g (85.8%), Anal. Calc. for $C_{19}H_{20}Br_2N_2O_4$: C, 45.62; H, 4.03; N, 5.60 Found: C, 45.66; H, 4.08; N, 5.62%. IR (KBr cm$^{-1}$)

selected bands: ν(C═N), 1648 vs, ν(C–$O_{phenolic}$) 1229 s, ν(O–H) 3430 s, $^1$H NMR (DMSO-$d_6$, 400 MHz): δ (ppm): 3.75 (s, 3H$^1$), 7.06–7.17 (m, 1H$^2$, 1H$^3$), 8.48 (m, 1H$^5$), 13.91 (m, 1H$^4$), 3.04–3.75 (s, 2H$^6$), 2.48 (s, 6H$^7$), $^{13}$C NMR (DMSO-$d_6$, 75.45 MHz): δ (ppm):54.94–56.46 (O-$^1$CH$_3$),117.23–150.18 (Arom-$^3$C-$^5$C),153.71 ($^7$C-OH), 165.77 ($^8$CH═N), 31.40 (-C-($^9$CH$_2$)$_2$), UV–Vis ($\lambda_{max}$ CH$_3$OH): 229 nm.

N,N′-bis(3-ethoxysalicylidene)-2,2-dimethyl-1,3-propanediamine ($H_2L^2$): Yield: 0.178 g (89.4%), Anal. Calc. for $C_{23}H_{30}N_2O_4$: C, 69.32; H, 7.59; N, 7.03 Found: C, 69.60; H, 7.62; N, 7.01%. IR (KBr cm$^{-1}$) selected bands: ν(C═N), 1638 vs, ν(C-$O_{phenolic}$) 1245 s, ν(O–H) 3436 s, $^1$H NMR (DMSO-$d_6$, 400 MHz): δ (ppm): 1.31–1.34 (s, 3H$^2$), 4.04 (H$^1$), 6.77–7.03 (m, 1H$^3$, 1H$^4$, 1H$^5$), 8.53 (m, 1H$^7$), 13.90 (m, 1H$^6$), 3.99 (s, 2H$^8$), 0.98 (s, 6H$^9$), $^{13}$C NMR (DMSO-$d_6$, 75.45 MHz): δ (ppm):15.2 ($^2$CH$_3$), 64.2–67.0 (O-$^1$CH$_2$),116.3–147.6 (Arom-$^4$C–$^6$C),152.2 ($^8$C-OH), 167.3 ($^9$CH═N), 24.0 ($^{11}$C-(CH$_3$)$_2$), 36.1 ((CH$_3$)$_2$-C-($^{10}$CH$_2$)$_2$), UV–Vis ($\lambda_{max}$ CH$_3$OH): 226, and 263 nm.

### 2.6. Synthesis of [Zn(L$^1$)(η$^1$-NCS)Pb(η$^1$-SCN)] (1)

$Zn(OAc)_2{\cdot}2H_2O$ (0.219 g, 1 mmol) was dissolved in 30 mL of hot methanol. Then a methanolic solution of the Salen ligand ($H_2L^1$) (0.502 g, 1 mmol) was added to it, followed by the drop-wise addition of an aqueous methanolic solution of NaSCN (0.0811 g, 1 mmol). The resultant mixture stirred for 1.5 h at room temperature. Then 15 mL methanol solution of $Pb(NO_3)_2$ (0.3312 g, 1 mmol) and five drops of acetonitrile (ACN) were added and started reflux for the overall mixture for the next 1 h 75 ℃. The bright yellow solution was filtered and kept refrigerated for crystallization. After a few days, block-sized, yellow-coloured single crystals suitable for SCXRD were obtained. Crystals were isolated by filtration and air-dried. Yield: 0.457 g, (59.8%), Anal. Calc. for $C_{21}H_{18}Br_2N_4O_4PbS_2Zn$: C, 28.44; H, 2.05; N, 6.32. Found: C, 28.47; H, 2.03; N, 6.35%. IR (KBr cm$^{-1}$) selected bands: ν(C═N), 1548 s, ν(NCS), 2093 s, ν(SCN), 2164 m, ν(Ar–O),1232 m, FT-Raman (cm$^{-1}$) selected bands: ν(C═N), 1632 s, ν(NCS), 2116 s, ν(SCN), 2190 m, $^1$H NMR (DMSO-$d_6$, 400 MHz): δ (ppm): 3.39 (s, 3H$^1$), 6.57–7.00 (m, 1H$^2$, 1H$^3$), 8.32 (m, 1H$^4$), 3.89–4.26 (s, 2H$^5$), 1.76–2.49 (s, 6H$^6$), UV–Vis $\lambda_{max}$ (DMSO): 374 nm.

### 2.7. Synthesis of [Cd(L$^2$)(η$^1$-NCS)Pb(η$^1$-SCN)]$_n$ (2)

We obtained 2 in a similar procedure as in the case of complex 1, using ligand ($H_2L^2$) (0.398 g, 1 mmol) and $Cd(OAc)_2{\cdot}2H_2O$ (0.269 g, 1 mmol) instead of $Zn(OAc)_2{\cdot}2H_2O$ After a few days, we got Block single-size crystals suitable for SCXRD. Filtration and isolated crystals air-dried. Yield: 0.779 g, (59.5%), Anal. Calc. for $C_{25}H_{28}Cd\ N_4O_4PbS_2$: C, 36.08; H, 3.39; N, 6.73. Found: C, 36.12; H, 3.41; N, 6.77%. IR (KBr cm$^{-1}$) selected bands: ν(C═N), 1670 vs, ν(NCS), 2066 s, ν(SCN), 2165 s, ν(Ar–O),1245, FT-Raman (cm$^{-1}$) selected bands: ν(C═N), 1632 vs, ν(NCS), 2091 s, ν(SCN), 2140 s, $^1$H NMR (DMSO-$d_6$, 400 MHz): δ (ppm): 1.21–1.78 (s, 3H$^2$), 3.81 (s, H$^1$), 6.54–7.02 (m, 1H$^3$, 1H$^4$, 1H$^5$), 8.47 (m, 1H$^6$), 3.37 (s, 2H$^8$), 0.03 (s, 6H$^9$), UV–Vis $\lambda_{max}$ (DMSO): 277, and 358 nm.

## 3. Results and discussion

### 3.1. Synthetic methodology

Two Salen ligands were synthesized based on the literature method (Scheme 1) [42a]. Lead complexes derived from Salen ligands were prepared in moderate good yield by selecting the more familiar *in situ* procedure (Scheme 1). Single crystals were not grown in methanol solvent; hence, we used few drops of acetonitrile to promote better diffracting-quality crystals suitable for SCXRD (Scheme 1). Two complexes are heteronuclear discrete and 1D polymer confirmed by SCXRD, being formulated as [Zn(L$^1$)(η$^1$-NCS)Pb(η$^1$-SCN)] **(1)** and [Cd(L$^2$)(η$^1$-NCS)Pb(η$^1$-SCN)]$_n$ **(2)**. Ligands and the corresponding complexes were characterized by elemental, EDX, PXRD, and various spectroscopic techniques. The compartmental $N_2O_4$ type Salen ligands disclose basic imitators since it encompasses two imines, two phenols, and two alkoxy groups. Two Salen ligand produces an $N_2O_2$ imine chelating position after deprotonation [58]. Tetradentate $N_2O_2$ imine chelating site and an additional $O_4$ compartment captured by Zn, Cd, and Pb ions in the presence of thiocyanate spacers (Scheme S2). However, several heteronuclear complexes have been synthesized by employing the referenced ligands [1,2,8–10,15a–d,59a–c]. But such hitherto Salen complexes promising cytotoxic behaviour towards human neuroblastoma cancer cell lines are even cramped in the literature.

### 3.2. Spectroscopic characterization

The IR spectroscopic tool characterized ligands and the complexes. The characteristic imine (C═N) stretching vibration of synthesized Salen ligand was located within the range 1648–1638 cm$^{-1}$ [60] (Fig. S1). In both complexes, the stretching vibration bands for FT-IR and Raman (C═N) are moved to 1548–1670 cm$^{-1}$ (for IR) (Fig. S2) and 1632 cm$^{-1}$ (for Raman) (Fig. S3). The above spectral data support the coordination of the azomethine nitrogen atom to the zinc and cadmium metal centre [61]. Thiocyanate counter anions (SCN$^-$) displayed strong bands in 2093, 2164 cm$^{-1}$ **(1)** and 2066, 2165 cm$^{-1}$ **(2)** (for IR) and 2116, 2190 cm$^{-1}$ **(1)**, 2091, 2140 cm$^{-1}$ **(2)** (for Raman). Therefore, splitting the thiocyanate peak is attributed to two distinct binding modes with the metal ions [62]. Ar–O stretching frequency near 1232–1245 cm$^{-1}$ is identical with reported Salen-type ligands. The UV–Vis absorption spectra of the Salen and the complexes have been performed in methanol and DMSO. Ligands exhibit three distinct bands at 229 nm and 226, 263 nm (Fig. S4), for π → π*/n → π* type transitions. In contrast, both complexes exhibit a strong ligand–based UV domain at 374 and 277, 358 nm (Fig. S5) because of the L → M charge-transfer transition (π → π*/n → π*) [61,63a,b]. Such spectral feature is identical to the reported Schiff base N,N′-bis(salicylidene)-1,3-diaminopentane [64a–d]. The presence of electron-withdrawing bromine and electron-donating ethoxy group result in a bathochromic shift of the absorption bands. The UV spectral domain supports the coordination mode of the Salen ligands with zinc and cadmium metal ions. Moreover, the credit of d$^{10}$ configuration and diamagnetic nature of zinc and cadmium metal ion, no metal centric d-d broad absorption band has been identified. The authenticate NMR spectroscopic tool characterized the Salen ligands and the complexes. The experimental section registered NMR spectral data of the as-synthesized compounds. Free Salen ligands in the region δ 5.0–8.0 ppm found no broad peak, suggesting the free –$NH_2$ group absence. The phenolic protons (OH$^4$/OH$^6$) are associated with the defined broad peak at δ 13.91 and 13.90 ppm. The protons (H$^5$/H$^7$) attached to the imino carbon are downfield shifted (δ 8.48–8.5 ppm) [64a–d] due to the influence of the combined effect of phenolic –OH and imino N groups in its close vicinity. The peaks within the range δ 7.06–7.17 and 6.77–7.03 ppm correspond to the aromatic protons (H$^2$-H$^3$/H$^3$-H$^5$). The three methyl protons (OCH$^1_3$) in ($H_2L^1$), attached to the aromatic oxygen, appear at δ 3.75 ppm whereas in ($H_2L^2$), (CH$^2_3$) and (O-CH$^1_2$) appear at 1.31–1.34 and 4.04 ppm. Protons (H$^9$) in the (C-(CH$_3$)$_2$ group appear at δ 0.98 ppm. Since methylene protons (H$^6$/H$^8$) are close to the imino nitrogen, they are de-shielded and appear at δ 3.04–3.75 ppm and 3.99 ppm (Fig.S6). Further, $^{13}$C NMR spectra of ligands showed the azomethine (CH═N) carbons at 167.77–176.30 ppm (Fig. S7). The other $^{13}$C important NMR peaks for Salen ($H_2L^1$) observed at 54.94–56.46 (O-CH$_3$), 117.23–150.18 (Arom-C), 153.71 (C-OH), 165.77 (CH = N), 31.40 (-C-($^9$CH$_2$)$_2$), and for Salen ligand ($H_2L^2$), 15.2 ($^2$CH$_3$), 64.2–67.0 (O-$^1$CH$_2$),116.3–147.6 (Arom-$^4$C–$^6$C),152.2 ($^8$C-OH), 167.3 ($^9$CH═N), 24.0 ($^{11}$C-(CH$_3$)$_2$, 36.1 ((CH$_3$)$_2$-C-($^{10}$CH$_2$)$_2$), ppm. Contrary to the heteronuclear Salen complexes, the coordination mode of azomethine nitrogen was assigned to the downfield shift of the azomethine proton signal from the ligand (8.48–8.53) to 8.32–8.47 ppm. The OH proton (OH$^4$/OH$^6$) signal at the ligands disappeared in the $^1$H

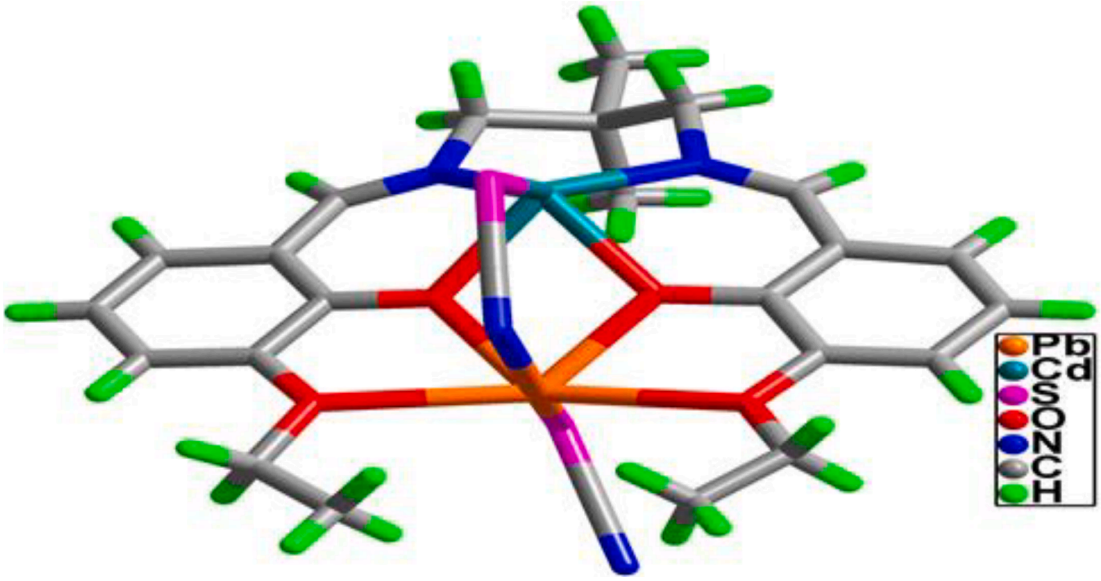


**Fig. 1.** The asymmetric unit of the complex 2.

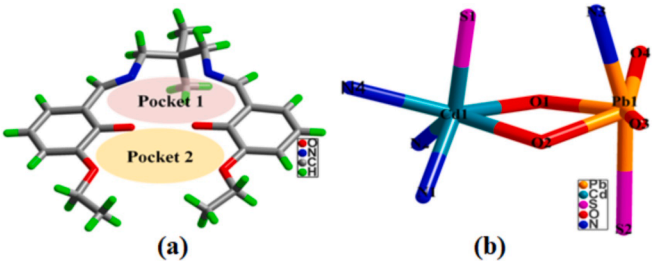


**Fig. 2.** (a) Two different pockets in ligand $[L^2]^{2-}$ and (b) bi-metallic clustered in 2.

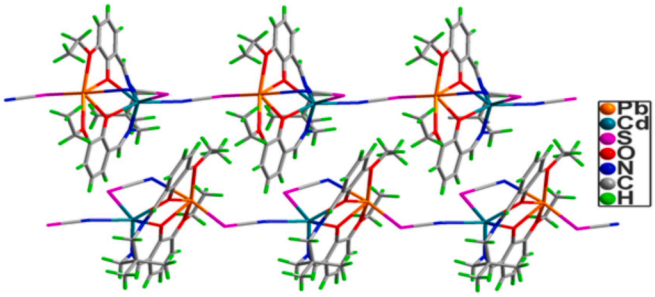


**Fig. 3.** The construction of the polymeric network of complex 2.

NMR spectra of the complexes, showing deprotonation and coordination of the oxygen with zinc and cadmium metal ion [64a–d] (Fig. S8).

### 3.3. EDX and PXRD

The chemical composition of the heteronuclear Salen complexes was analyzed by employing EDX experiments. The EDX profile confirmed the chemical composition of both complexes, where the weight percentage (%) contribution of the elements is presented in Table S4. The calculated and EDX values of essential elements (C, N, O, S, and Br) present are good in agreement. Thus, the EDX profile contained only essential predictable elements. EDX profile also represents metals like Cd, Zn, and Pb, which further agreed with the empirical formula of the complexes. At room temperature, recorded PXRD patterns of the Salen complexes within the range ($2\theta = 40^0$–$50^0$) at a wavelength ($\lambda$) of 1.54 Å. Because of their crystalline existence, Fig. S9A-9B displayed well-defined sharp PXRD peaks. PXRD observed patterns of the complex's bulk materials are like the patterns simulated from SCXRD CIF data. Therefore, the single crystals and the bulk material are the same. The PXRD analytical results will confirm the phase purity of each bulk sample.

## 4. Crystal structure description

### 4.1. Crystal structure of **2** and **1**

The X-ray single-crystal analysis divulges that complex **2** crystallizes in the orthorhombic space group ($P\ 2_12_12_1$, $Z = 4$). The asymmetric unit comprises two crystallographic independent different Pb(II) and Cd(II) metal ions, with full occupancy. The crystal structure of **2** is built from a fully deprotonated form of $[L^2]^{2-}$ and the two thiocyanate spacers. Thereby formation of the heteronuclear asymmetric unit of $[Cd(L^2)(\eta^1\text{-}NCS)Pb(\eta^1\text{-}SCN)]_n$ **(2)** (Fig. 1). The asymmetric unit is electronically neutral. The four cationic charges are balanced by the two anionic charges of $[L^2]^{2-}$ and the two more anionic charges from the two thiocyanate co-ligands. Substantial bond distances and angles are gathered in the supplementary electronic material (Table S1). The ORTEP diagram of the complex is shown in Fig. S10.

From the design point of view, the ligand $[H_2L^2]$ contains two pockets, 1 and 2 (Fig. 2a). The former pocket is constructed from 2 N and 2O, and the second pocket comprises 4O atoms. Both the pockets can accommodate metal ions towards the building up the bi-metallic clustered. While the reaction, the hydroxyl groups (–O1H and –O2H) are positioned towards each other becomes deprotonated and holds the two metal ions, cadmium (inner core) of $[L^2]^{2-}$ and lead (outer core) of $[L^2]^{2-}$ through η2 manner. Herein, the competitive occupancy of Cd vs. Pb is one of the exciting aspects of stereochemistry. Cd(II) occupying inner $N_2O_2$, and Pb(II) occupying the outer $O_4$ compartments. The significant Pb(II) ionic radius (133 pm) is much larger than Cd metal ions (109 pm). Therefore, it is difficult for Pb(II) to be accommodated in the inner $N_2O_2$ compartment, where minor metal Cd(II) fits well at the outer $O_4$ cavities. Hence Pb(II) ion provides well in the open external $O_4$ pit [65]. Such stereochemical preference of Pb is also valid for complex **1** (Zn, ionic radius 88 pm). The two thiocyanate anions are linked with Cd and Pb metal ions in opposite directions. Such binding leads to form a bi-nuclear heterometallic cluster (Fig. 2b).

**Table 2**
Possible interaction parameters in **2–1**.

| Components for complex **2** | Bond distance (Å) | Bond angle (°) |
|---|---|---|
| C7-H7·····S1 | 3.0992(47) | 171.96(72) |
| C5-H5·····N4 | 3.0486(130) | 143.831(840) |
| C8-H8A···· | 3.1227(131) | 153.288(799) |
| C20-H20A·····Cg(C1-C6) | 2.6431(1) | 166.322(796) |
| Components for complex **1** | Bond distance (Å) | Bond angle (°) |
| C9AA-H9AA·····S1 | 3.0290(17) | 154.594(395) |
| C4BA-H4BA·····Cg(C5-C9) | 2.8699(1) | 162.601(395) |
| CA-HA·····S1 | 2.9206(17) | 174.444(424) |

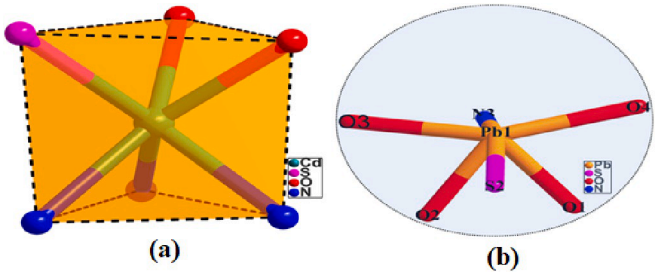


**Fig. 4.** (a) Six coordination trigonal prismatic geometry around cadmium and (b) Hemi- directed six coordinated Sphere around lead.

Crystal structure **2** discloses it contains two thiocyanates ion. One of the thiocyanate ligands is acting as a bridge between lead (via S donor atom of SCN) and cadmium ions (through N donor atom of NCS) to form a 1D coordination polymer (Fig. 3). The nitrogen atom of the thiocyanate ligand of the asymmetric unit is linked to the cadmium ion of the nearby unit is due to the vacant coordination site on cadmium. Though the Pb ion can connect with nitrogen, such a binding fashion will bring the two units close enough to cause severe steric crowding between the ethyl groups on each unit, and the resulted polymeric architect becomes unstable. The two nearest polymeric 1D chains undergo the number of non-covalent interactions (S···H, hydrogen bonding, etc. Table 2) to form a 2D network (Fig. S11) [66]. Herein the structural discussion relying on Shimoni-Livny et al. is fascinating in connection to Hemi-directed nature Pb(II) ion [67]. The Hemi-coordinated Pb(II) centre has a significant void opposite to the ligand thiocyanate. Such an environment is similar to other Pb(II) complexes [68]. All bonds around the Pb(II) atom are concentrated within less than one hemisphere of the coordination sphere, leaving a large gap on the Pb(II) ion. Therefore, it allows close interaction with the S atom (S1) of the thiocyanate from an adjacent molecule.

The coordination fashion of the ligands in **2** is presented in Fig. S12a. The ligand $[H_2L^2]$ is bound to the metal ions through $\eta$1-oxygen, $\eta$2-oxygen, and $\eta$1-nitrogen, and both the thiocyanates are showing $\mu$2-$\eta$1:$\eta$1 fashion. Out of the two thiocyanate ligands, one thiocyanate is attached in a cis manner to the two metal ions present within the asymmetric unit (Fig. S12c). The other thiocyanate ligand is linked in trans fashion to the two metal ions present in the two different units (Fig. S12b). The ligands' coordination furnished the six coordination of the cadmium metal ion with trigonal prismatic geometry, comprising 3O, 2N, and one S atom. The lead ion in this complex is six coordinated with the classical Hemi-directed coordination sphere (Fig. 4) (Table S2). The lead metal ion is a post-transition element, and the (+2) oxidation state in this complex with electronic configuration is $[Xe]4f^{14}5d^{10}6s^2$ and exhibits an inert-pair effect. The 6 $s^2$ electron is inert to participate in the oxidation state process/covalent bond formation. It behaves as lone pair, which causes the non-spherical charge allocation around the lead ion, i.e., the distribution of ligands around the lead leaves some vacant space (identifiable void). Thus, the lead (II) ion in this complex preferred the Hemi-directed coordination sphere over the Holo-directed coordination sphere [39–41].

Interestingly, by keeping the same design policy of the ligand $[H_2L^2]$ (pocket strategy), we have utilized another new ligand $[H_2L^1]$ (Fig. S13) for the synthesis of 1 after utilizing the thiocyanate counter anion. 1 crystallizes in the monoclinic space group (P 1 21/n 1, Z = 4). The ORTEP diagram of the complex is shown in Fig. S10. It contains two crystallographically independent zinc and lead metal ions with the asymmetric unit formula $[Zn(L^1)(\eta^1\text{-NCS})Pb(\eta^1\text{-SCN})]$ **(1)** (Fig. S14). Keeping in mind that the binding fashion of thiocyanate anion in this complex, the Pearson theory [69] holds very well between $Zn^{2+}$ and $Pb^{2+}$ ion, the former is a hard acid, and the latter is a soft acid. Thus, the S atom (soft base) of thiocyanate is linked to the soft acid ($Pb^{2+}$), and the N atom (hard base) of thiocyanate is connected to the hard acid ($Zn^{2+}$) (Fig. 6). Herein the M–Pb (M = Cd/Zn) bond distances [3.726–3.540 Å] are comparable with the literature-reported heteronuclear Pb(II) complexes [1,2,8–10,15a–d,59a–c]. Moreover, Pb-N, Pb-O, and Pb-S (SCN) bond distance values rejected the Tetrel bonding concept, one of the popular bonding features for the literature reported Pb(II) complexes (Table S3). Unlike 2, 1 is a discrete network (Fig. S15). The probable reason would be that large-sized bromine will create a steric hindrance

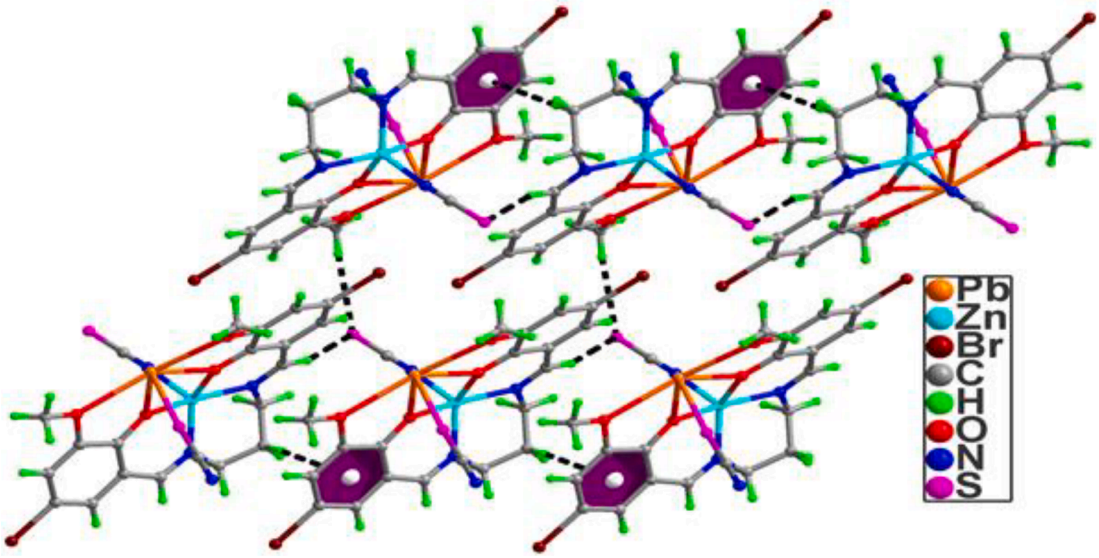


**Fig. 5.** The presence of non-covalent interaction in 1.

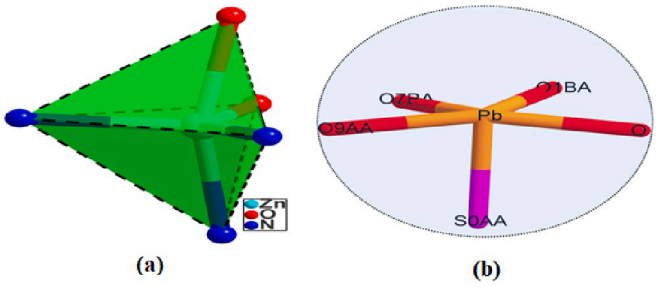


**Fig. 6.** (a) Five coordinated trigonal bipyramid geometries around zinc metal ion and (b) Hemi-directed five coordination Sphere around lead.

when two of such units come close together to form a polymeric network. But two of such nearby discrete units undergo non-covalent interaction to develop a 1D framework (Fig. 5, Table 2).

$H_2L^1$ is bound to the metal ions through $\eta^1$-oxygen, $\eta^2$-oxygen, and $\eta^1$-nitrogen, and both the thiocyanate ligands are showing $\mu1$-$\eta^1$ fashion (Fig. S16). The Addison structural parameter ($\tau$) [70] value helps to determine the correct stereochemical environment around the Zn metal ions, $(\tau = (\beta - \alpha)/60^0$ where $\beta$ and $\alpha$ are the two largest angles around the central atom: $\tau = 0$ for perfect square pyramidal and 1 for an ideal trigonal geometry). Zinc metal ions are five coordinated trigonal bipyramidal ($\tau = 0.29$), fulfilled by binding action from 2O and 3N (Fig. 6a). Though the lead ion is Penta-coordinated, it is showing classical Hemi-directed coordination sphere (Fig. 6b) over Holo-directed coordination sphere (reason vide supra) (Table S2).

### 4.2. Cambridge structural database studies

We found that in 2, Cd-NCS is preferred binding over Cd-SCN, further confirmed from CSD literature studies and Cd–N–C angle value. It is well-known that the CSD is a convenient and reliable tool for analyzing geometrical parameters. According to the Cambridge Structural Database (CSD) literature search, to better understand the different binding modes of the thiocyanate anion (N or S) with metal ions [25]. According to literature, we have found only 17 X-ray structures and a total of 23 fragments where the $SCN^-$ is coordinated to Cd···SCN fashion. Reported literature eliminated those hits where the $SCN^-$ is a bridging ligand in any two modes represented in Histogram (Fig. S16B). Histogram (Fig. S16B), 186 X-ray structures (257 fragments) were found where the $SCN^-$ is coordinated to Cd through the N atom. The histogram plots show a preference for coordination via the nitrogen atom due to the more significant number of hits observed for this coordination mode. Another exciting aspect is the different coordination angle kept at 65 for

**Table 3**
DFT calculated different quantum chemical parameters.

| Basis Set | $E_{HOMO}$ | $E_{LUMO}$ | I | A | ΔE | η | σ | χ | Pİ | ω | ε | dipol | Energy |
|---|---|---|---|---|---|---|---|---|---|---|---|---|---|
| 1. B3LYP/Lanl2dz LEVEL | | | | | | | | | | | | | |
| 1 | −5.3626 | −2.6754 | 5.3626 | 2.6754 | 2.6871 | 1.3436 | 0.7443 | 4.0190 | −4.0190 | 6.0110 | 0.1664 | 6.4525 | −39355.1339 |
| 2 | −3.6532 | −2.5413 | 3.6532 | 2.5413 | 1.1119 | 0.5559 | 1.7988 | 3.0972 | −3.0972 | 8.6277 | 0.1159 | 5.3571 | −40390.6853 |
| 2. HF/Lanl2dz LEVEL | | | | | | | | | | | | | |
| 1 | −8.0563 | 0.8988 | 8.0563 | −0.8988 | 8.9551 | 4.4775 | 0.2233 | 3.5787 | −3.5787 | 1.4302 | 0.6992 | 7.9330 | −39046.9635 |
| 2 | −6.6032 | 1.8210 | 6.6032 | −1.8210 | 8.4242 | 4.2121 | 0.2374 | 2.3911 | −2.3911 | 0.6787 | 1.4735 | 5.7013 | −40091.1053 |
| 3. M062X/Lanl2dz LEVEL | | | | | | | | | | | | | |
| 1 | −6.7204 | −1.7037 | 6.7204 | 1.7037 | 5.0167 | 2.5084 | 0.3987 | 4.2121 | −4.2121 | 3.5365 | 0.2828 | 6.2663 | −39333.0108 |
| 2 | −5.0061 | −1.1437 | 5.0061 | 1.1437 | 3.8624 | 1.9312 | 0.5178 | 3.0749 | −3.0749 | 2.4480 | 0.4085 | 6.7394 | −40370.3707 |

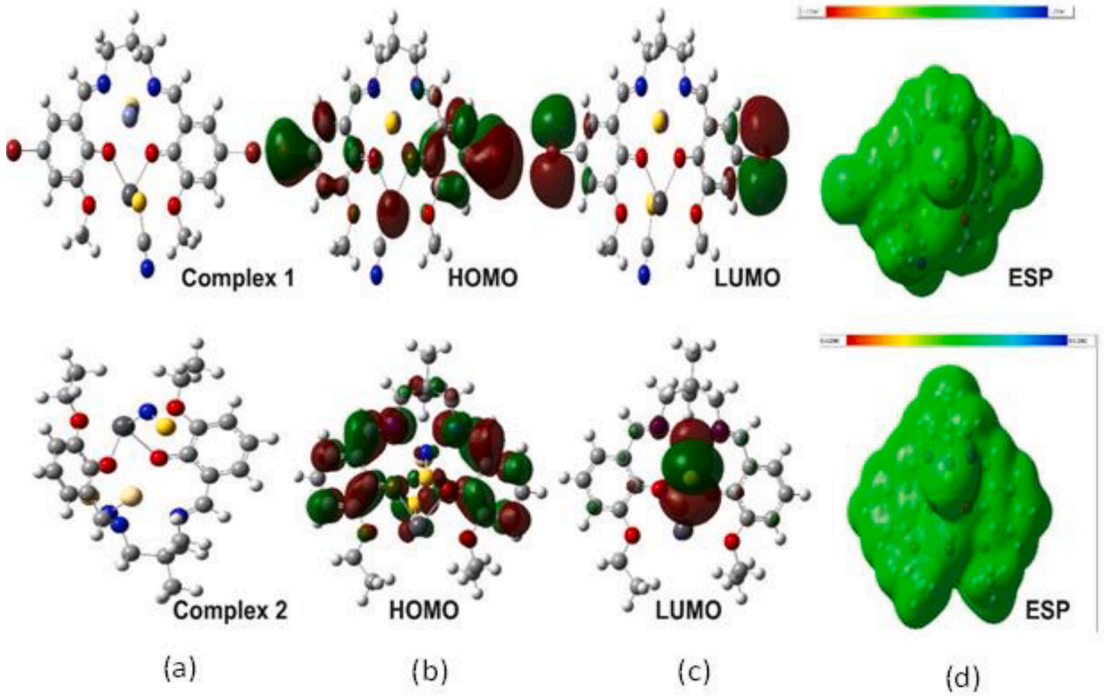


**Fig. 7.** (a) DFT optimized complex structures, (b) HOMO shape of the complexes, (c) LUMO shape of the complexes, and (d) ESP of the metal complexes.

each type of complex. In the Cd–SCN histogram plot, it can be regarded a preference for a Cd–S–C angle between 90 and 110°, and in the Cd–NCS plot, a more comprehensive range of values is observed centred around a Cd–N–C angle of 155°. In our complex 2, Cd–N–C angle is observed near 159°, supported by Cd-NCS bonding fashion.

## 5. FMO approach

The quantum chemical DFT has become a used method for bleaching both the chemical and biological activities of the synthesized complexes. All quantum chemical parameters obtained employing Gaussian calculations based on different basis sets are shown in Table 3. The DFT calculated parameters provide information about the properties of the complexes and are used to compare their reactivities. Among the different quantum chemical parameters, first is the FMO approach, where the two most important parameters are HOMO (highest occupied molecular orbital) and LUMO (lowest unoccupied molecular orbital). These two parameters are the best known among quantum chemical parameters. Although the numerical value of the HOMO parameter of the metal complexes does not explain the activation of the other metal complexes, it provides crucial information. The numerical value of the HOMO parameter indicates the metal complex's ability to donate electrons to establish a chemical bond. The chemical activity of the metal complexes with the highest HOMO energy numerical value of the metal complexes is the highest. However, the LUMO energy value of metal complexes show their ability to accept electrons to establish a chemical bond [71]. The chemical activity of the metal complexes with the lowest LUMO energy numerical value of the metal complexes is the highest. Another important calculated parameter is ΔE, where $\Delta E = E_{HOMO} - E_{LUMO}$. The complex's optimized geometry, HOMO, and LUMO shape are presented in Fig. 7. The molecule with the smallest numerical value of this parameter has the highest chemical activity. When the HOMO energy values of 1 and 2 are compared, it is seen that the 2 is higher than 1. Therefore, the chemical reactivity of 2 is more elevated. According to the LUMO energy value of the complexes, the activity is higher because the LUMO energy value of 1 is lower than the LUMO energy value of 2. Another parameter is the ΔE. Since the energy value of the ΔE parameter of 2 is more petite than 1, the reactivity is maximum for 2.

Some of the quantum chemical parameters computed have their formal representations. In Fig. 7, the optimized structures of the metal complexes are given in the first picture. The second picture shows the HOMO shapes of the metal complexes. It has been shown which atoms the HOMO orbitals are. In the third picture, the LUMO shapes of the metal complexes are given. In the fourth and last picture, ESP (Electrostatic Potentials) pictures of metal complexes are given. ESP pictures are colourful. The electron density of the red colour is the highest, while the electron density of the blue colour is the least [72a,b].

### 5.1. Global chemical parameters

Apart from FMO, the global quantum chemical parameters are also calculated, favouring the Lead metal complexes. The global chemical parameters are used to explain the reactivities of the complexes. One of these estimated parameters is electronegative χ, a numerical expression of the ability of molecules to attract bond electrons. As the electronegative value of a complex increases, its chemical activity will decrease as it will attract more electrons required for chemical interaction. Analysis observed that the numerical value of the electronegativity parameter of **1** is higher than **2**. Another parameter is the chemical hardness, symbol η, which refers to the resistance to changing the electron cloud density in a chemical system. The opposite of this situation is softness. According to Table 3, it is seen that the chemical hardness of 1 is higher than **2**. Hence complex **1** makes it more susceptible to nucleophilic attack.

**Table 4**
Molecular docking $E_{total}$ energy value of the complexes.

| Complex | Proteins | | |
|---|---|---|---|
| | Breast cancer | Liver cancer | Lung cancer |
| 1 | −310.30 | −337.36 | −290.11 |
| 2 | −281.87 | −323.64 | −297.56 |

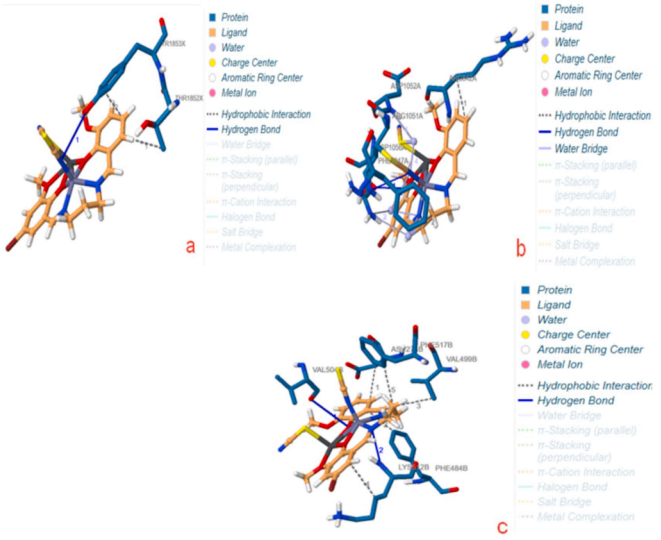


**Fig. 8.** Representation of the interaction of the metal complex 1 with breast cancer (a), liver cancer, and (b) with lung cancer (c).

### 5.2. Molecular docking

We consider the molecular docking calculations to compare the biological activities of the complexes. The docking experiments compare the activities of the metal complexes against the cancer proteins. The cancer proteins used are the crystal structure of the BRCT repeat region from the breast cancer-associated protein, crystal structure of VEGFR kinase (liver cancer) protein, and crystal structure of an allosteric Eya2 phosphatase inhibitor (lung cancer) protein. Many parameters are calculated because of the interaction of these proteins and the complexes. The most important among these parameters is the total energy (Table 4). The molecule with the most negative numerical value of this parameter has the highest biological activity [72a,b]. The most important factor affecting the numerical value of this parameter is the interactions between the metal complexes and the proteins. These interactions nature is all chemical, and it observed that as the chemical interactions between metal complexes and the proteins increase, the activities of the complexes increase. These chemical interactions are H-bonds, polar and hydrophobic exchanges, π-π, and halogen [72a,b]. The interaction of the metal complex with breast cancer, liver cancer, and lung cancer is described in Fig. S17(a–c).

### 5.3. Protein-Ligand interaction Profiler (PLIP)

Since molecular docking calculations are made with the HEX 8.0.0 program, this does not provide detailed interaction pictures. Therefore, to examine the interaction of proteins with the metal complexes, we conducted a Protein-Ligand Interaction Profiler (PLIP). In such a high-profile analysis, the chemical interactions between metal complexes and the proteins are specified in Fig. 8 which shows the interactions of complex 1, which has the highest activity, with cancer proteins, according to the interactions between metal complexes and proteins. In Fig. 8a–c, we see complex 1 with cancer protein interactions. Herein the metal complexes form hydrophobic interaction with proteins and

**Table 5**
Hydrophobic Interactions of protein and the metal complex.

| Index | Residue | AA | Distance | Ligand atom | Protein atom |
|---|---|---|---|---|---|
| Breast cancer with complex **1** | | | | | |
| 1 | 1852X | THR | 3.53 | 1990 | 1777 |
| 2 | 1853X | TYR | 2.87 | 1992 | 1789 |
| Liver cancer with complex **1** | | | | | |
| 1 | 842A | ARG | 3.16 | 3147 | 287 |
| 2 | 1047A | PHE | 3.81 | 3134 | 1782 |
| Lung cancer with complex **1** | | | | | |
| 1 | 274B | ASP | 3.42 | 7239 | 98 |
| 2 | 484B | PHE | 2.91 | 7237 | 1924 |
| 3 | 499B | VAL | 3.58 | 7228 | 2066 |
| 4 | 512B | LYS | 3.49 | 7216 | 2109 |
| 5 | 517B | PHE | 3.38 | 7228 | 2162 |

hydrogen bond interactions. On the other hand, in Fig. 10b, it is seen that 1 creates hydrophobic interaction, hydrogen bond, and water bridge interactions with liver cancer protein.

The interactions occurring in the calculations made with Protein-Ligand Interaction Profiler analysis are given in Fig. 8 in detail. The chemical interactions that occur in these pictures are given in detail in Table 5–7. These tables show which interactions mediate between complexes and proteins. There are many interactions, such as Hydrophobic Interactions [72a,b,73]. These interactions are the most common because the software does not generate any information related to hydrophilicity or hydrophobicity.

### 5.4. Anti-proliferative activity of compounds

The cell viability assay (MTT) was performed on SH-SY5Y cells, which were exposed to the test samples for 24 h with a concentration range of 1.25 to 40 μM (Fig. 9). A consistent cytotoxic activity was found in *C*2 against the neuroblastoma cells with an $IC_{50}$ concentration of 3.91 ± 1.07 μM. While as, C1 also registered cell death with an $IC_{50}$ 8.18 ± 1.09 μM (Table 8). With increasing concentration (1.25–40 μM), the death rate of cancer cells increased, as shown in the microscopic investigation. The analyses confirmed that the ligands and metal salts had low cytotoxicity at 1.25–10 μM concentration (Fig. 9). Zinc acetate had 30.59% and 41.1% cell death at 20 μM and 40 μM concentrations. As per the previous literature, zinc acetate is known to have cytotoxic effects [74a,b]. Interestingly, the metal salts and ligands alone did not show high cytotoxicity, but the C1 and C2 prepared from these components enhanced the cytotoxicity in neuroblastoma cells. The microscopic images of the neuroblastoma cells treated with C1 and C2 showed significant cell death compared to the untreated control cells (Fig. S18). The data showed that C1 and C2 possess potent anticancer abilities and cytotoxic effects are comparable to the cancer drug cisplatin [75].

### 5.5. Intracellular ROS generation and mitochondrial membrane potential (MMP)

An increasing number of therapeutic strategies are being used to induce oxidative stress incompatible with cellular life causing cancer cell death [76]. Therefore, ROS generation was fulfilled in SH-SY5Y cells after treating with C1 and C2. The data exhibited three-fold and four-fold enhanced ROS levels in the cells treated with C1 and C2, respectively, compared to untreated cells (Fig. 10A). Oxidation of the mitochondrial membrane (pore formation) due to rapid ROS production leads to dysfunction of the MMP, which is a well-known marker of apoptosis [73]. The results depicted a 49.25% decrease in Rh123 fluorescence in cells treated with C2, while for C1 treated SH-SY5Y cells showed 39.99% mitochondrial damage compared to untreated cells (Fig. 10B). Thus, the enhanced ROS generation and mitochondrial depolarization in SH-SY5Y cells following compound treatment indicate

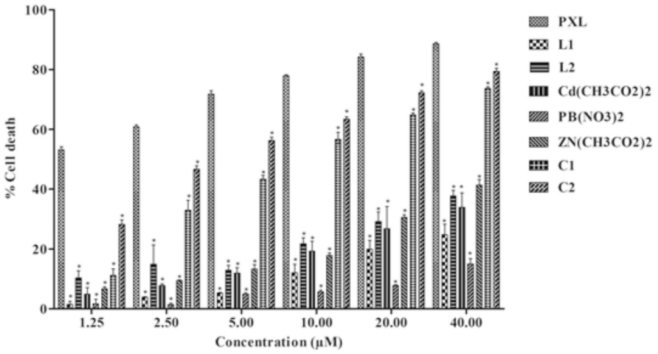


**Fig. 9.** Effect of ligands, metal salts and complexes at a concentration of 1.25–40 μM on SH-SY5Y cells. Data was presented as mean ± SEM ($n = 3$). Paclitaxel was used as a standard drug. Statistical significance was assessed one-way ANOVA followed by one sample t's test. *$p < 0.05$ was considered as significant.

**Table 6**
Hydrogen Bonds of protein and the metal complex.

| Index | Residue | AA | Distance H-A | Distance D-A | Donor angel | Protein donor | Side chain | Donor Atom | Acceptor Atom |
|---|---|---|---|---|---|---|---|---|---|
| Breast cancer with complex **1** | | | | | | | | | |
| 1 | 1853X | TYR | 3.28 | 3.72 | 110.00 | √ | √ | 1791 [O3] | 2000 [N1] |
| Liver cancer with complex **1** | | | | | | | | | |
| 1 | 1051A | ARG | 3.20 | 3.65 | 108.85 | √ | √ | 1811 [Ng+] | 3155 [N3] |
| 2 | 1056A | ASP | 3.72 | 4.04 | 103.57 | √ | √ | 1872 [O3] | 3153 [O2] |
| Lung cancer with complex **1** | | | | | | | | | |
| 1 | 504B | VAL | 3.63 | 3.91 | 100.38 | | | 7246 [O2] | 2099 [O2] |
| 2 | 512B | LYS | 3.49 | 4.08 | 119.26 | √ | | 2104 [N3] | 7224 [N2] |

**Table 7**
Water bridges of protein and the metal complex.

| Index | Residue | AA | Distance H-A | Distance D-W | Water angel | Protein donor | Donor Atom | Acceptor Atom | Water Atom |
|---|---|---|---|---|---|---|---|---|---|
| Liver cancer with complex **1** | | | | | | | | | |
| 1 | 1051A | ARG | 2.71 | 3.56 | 150.88 | 80.19 | √ | 1814 [Ng+] | 3130 [N2] |
| 2 | 1051A | ARG | 3.62 | 4.01 | 124.75 | 103.32 | √ | 1814 [Ng+] | 3155 [N3] |
| 3 | 1051A | ARG | 2.65 | 4.01 | 124.75 | 94.67 | √ | 1814 [Ng+] | 3130 [N2] |
| 4 | 1052A | ASP | 2.97 | 3.11 | 153.80 | 73.97 | √ | 1821 [Nam] | 3155 [N3] |

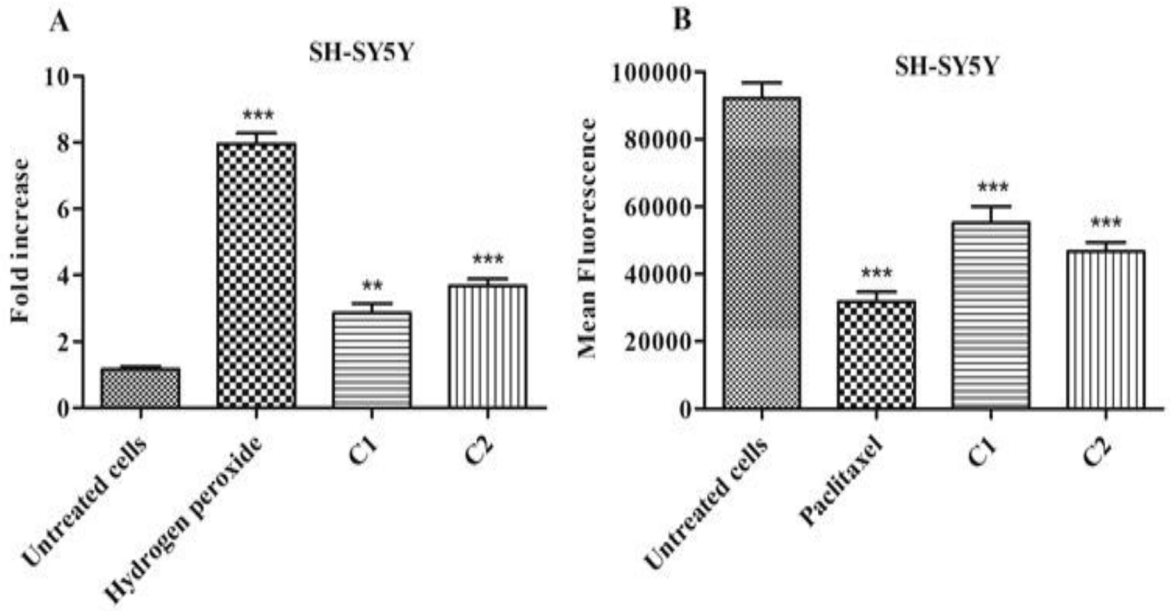


**Fig. 10.** Intracellular ROS generation (A) and MMP analysis (B) in SH-SY5Y cells after 4 h exposure with the synthesized compounds (10 μM) and positive control (Paclitaxel, 1 μM). Results represented as mean ± SEM of three different experiments. Data was statistically significant with $^{*}p < 0.05$, $^{**}p < 0.01$, $^{***}p < 0.001$ when compared with control.

**Table 8**
Effect of ligands, free metal salts and complexes on SH-SY5Y cells. Data was expressed as $IC_{50}$ value (mean ± SEM) of three independent experiments.

| Sl. No. | Compounds | $IC_{50}$ (μM) values against SH-SY5Y cells |
|---|---|---|
| 1. | Paclitaxel | 1.03 ± 1.05 |
| 2. | C1 | 8.18 ± 1.09 |
| 3. | C2 | 3.91 ± 1.07 |
| 4. | $H_2L^1$ | 158.1 ± 1.32 |
| 5. | $H_2L^2$ | 112.2 ± 1.39 |
| 6. | $Cd(OAc)_2{\cdot}2H_2O$ | 105.5 ± 1.36 |
| 7. | $Pb(NO_3)_2$ | 445.9 ± 1.46 |
| 8. | $Zn(OAc)_2{\cdot}2H_2O$ | 65.82 ± 1.08 |

apoptosis in these cells.

### 5.6. Western blot analysis

Further, to evaluate the apoptotic pathway activated by C1 and C2, activation of caspase-3 was analyzed. The western blot analysis revealed activation of caspase-3 in C1 and C2 treated SH-SY5Y cells (Fig. 11A). The densitometric analysis (Fig. 11B) revealed lowered caspase-3 expression following C1 (~0.7fold) and C2 (0.8fold) treatment. Caspases, a group of cysteine proteases that can cleave many cellular substrates to dismantle cell contents, play a vital role in apoptosis [77,78]. Cleavage of caspase-3 plays a fundamental role in the execution of the apoptotic process. Collectively, the results indicate the induction of apoptotic pathways *via* C1 and C2 in neuroblastoma cells.

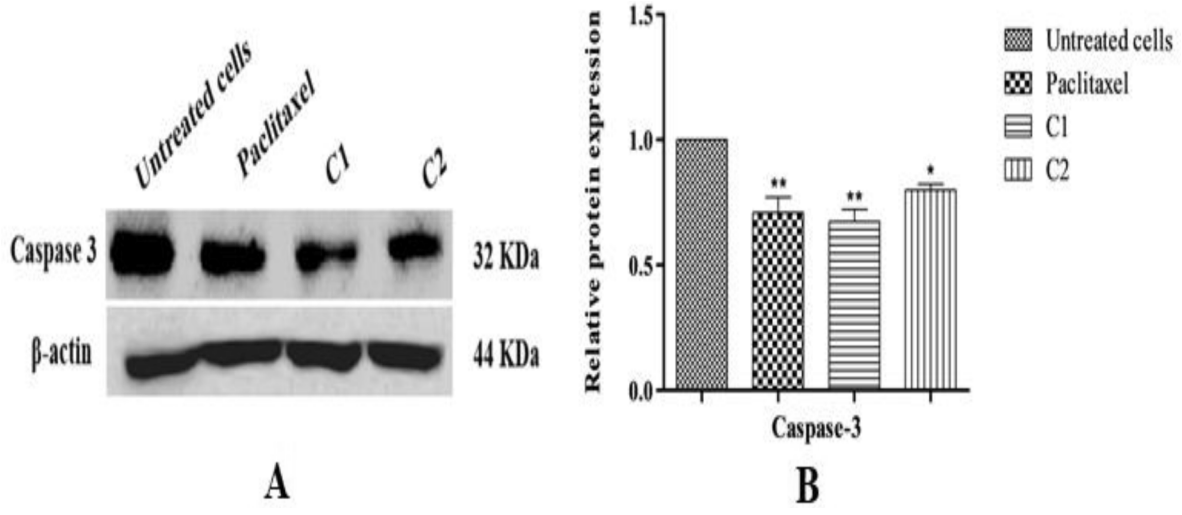


**Fig. 11.** Western blot analysis of activated caspase-3 in lysates of SH-SY5Y cells treated with complexes (A). Paclitaxel (1 μM) treated and untreated cells were used as positive and negative controls, (B). The intensity of caspase-3 was quantitated by densitometry and shown in the bar graph after normalizing the intensity values with corresponding β-actin expression (n = 3).

## 6. Conclusions

In summary, we have synthesized and characterized two hetero-bimetallic Lead compounds, viz. [Zn($L^1$)(η1-NCS)Pb(η1-SCN)] (1) and [Cd($L^2$)(η1-NCS)Pb(η1-SCN)]$_n$ (2). SC-XRD confirmed a de-protonated form of Salen ligands encapsulated by M(II) ions into the $N_2O_2$ compartment (M = Zn/Cd) but the better placement of Pb(II) ions by outer $O_4$ cavities. The stereochemical position of Pb(II) ions is Hemi-directional. FMO, Molecular docking, and PLIP have been implemented to underpin the experimental and theoretical biological findings. We investigated *in vitro* cytotoxic effects of the complexes, free ligands, and metal salts against neuroblastoma cancer cells. The observed $IC_{50}$ values 8.18 ± 1.09 μM and 3.91 ± 1.07 μM, declared the selectivity of the complexes, which was comparable with the standard drug *cisplatin*. The cytotoxic results revealed that the metal salts and Salen ligands alone did not show high cytotoxicity. The complexes C1 and C2 prepared from these components enhanced the cytotoxicity in neuroblastoma cells. We explained the mechanistic perception of cytotoxic response, apoptosis cancer cell death via intracellular ROS generation, and mitochondrial membrane potential (MMP). The enhanced ROS generation and mitochondrial depolarization explore the apoptosis in these cells. Further, to examine the apoptotic pathway, we also intended the Western blot-activated caspase-3 in the lysates of SH-SY5Y cells. The results imply the induction of apoptotic pathways via **1** and **2** in neuroblastoma cells. Research on Lead compounds in neuroblastoma cancer cell lines opens a new window to encourage re-evaluation of the compounds as anti-tumour agents.

## Declaration of Competing Interest

The authors declare that they have no known competing financial interests or personal relationships that could have appeared to influence the work reported in this paper.

## Acknowledgements

This research work did not receive any specific grant from funding agencies in public, commercial or non-profit sectors. Dr. Dipankar Mishra gratefully acknowledges the financial grant sanctioned by UGC, New Delhi, in his favour vide Minor Research Project (F.PSW-232/15-16 (ERO).

## Appendix A. Supplementary data

Supplementary data to this article can be found online at https://doi.org/10.1016/j.poly.2021.115504.

## References

[1] P.K. Bhaumik, A. Banerjee, T. Dutta, S. Chatterjee, A. Frontera, S. Chattopadhyay, CrystEngComm 22 (2020) 2970–2977.
[2] A. Hazari, L.K. Das, A. Bauzá, A. Frontera, A. Ghosh, Dalton Trans. 45 (2016) 5730–5740.
[3] P. Seth, S. Giri, A. Ghosh, Dalton Trans. 44 (2015) 12863–12870.
[4] S. Yamada, Coord. Chem. Rev. 190 (1999) 537–555.
[5] L.S. Felices, E.C. Escudero-Adán, J. Benet-Buchholz, A.W. Kleij, Inorg. Chem. 48 (2009) 846–853.
[6] S.A. Fairhurst, D.L. Hughes, G.J. Leigh, J.R. Sanders, J. Weisner, J. Chem. Soc. Dalton Trans. (1994) 2591–2598.
[7] R.M. Clarke, T. Storr, Dalton Trans. 43 (2014) 9380–9391.
[8] X. Yang, R.A. Jones, S. Huang, Coord. Chem. Rev. 273–274 (2014) 63–75.
[9] S. Roy, M.G.B. Drew, A. Bauzá, A. Frontera, S. Chattopadhyay, Dalton Trans. 46 (2017) 5384–5397.
[10] S. Roy, A. Bhattacharyya, S. Purkait, A. Bauzá, A. Frontera, S. Chattopadhyay, Dalton Trans. 45 (2016) 15048–15059.
[11] A. Bhattacharyya, S. Roy, J. Chakraborty, S. Chattopadhyay, Polyhedron 112 (2016) 109–117.
[12] P. Bhowmik, S. Jana, P.P. Jana, K. Harms, S. Chattopadhyay, Inorg. Chim. Acta. 390 (2012) 53–60.
[13] P. Bhowmik, S. Jana, P.P. Jana, K. Harms, S. Chattopadhyay, Inorg. Chem. Commun. 18 (2012) 50–56.
[14] (a) V. Vieru, T.D. Pasatoiu, L. Ungur, E. Suturina, A.M. Madalan, C. Duhayon, J.-P. Sutter, M. Andruh, L.F. Chibotaru, Inorg. Chem. 55 (2016) 12158;
(b) M.-J. Liu, K.-Q. Hu, C.-M. Liu, A.-L. Cui, H.-Z. Kou, New J. Chem. 40 (2016) 8643;
(c) T.D. Pasatoiu, C. Tiseanu, A.M. Madalan, B. Jurca, C. Duhayon, J.P. Sutter, M. Andruh, Inorg. Chem. 50 (2011) 5879.
[15] (a) C.-L. Hu, J.-G. Mao, Coord. Chem. Rev. 288 (2015) 1–17;
(b) G.N.D. Francesco, A. Gaillard, I. Ghiviriga, K.A. Abboud, L.J. Murray, Inorg. Chem. 53 (2014) 4647–4654;
(c) K. Ghosh, S. Roy, A. Ghosh, A. Banerjee, A. Bauzá, A. Frontera, S. Chattopadhyay, Polyhedron 112 (2016) 6–17;
(d) D. Sadhukhan, A. Ray, G. Pilet, C. Rizzoli, G.M. Rosair, C.J. Gomez- García, S. Signorella, S. Bell, S. Mitra, Inorg. Chem. 50 (2011) 8326–8339.
[16] S. Roy, A. Dey, M.G.B. Drew, P.P. Ray, S. Chattopadhyay, New J. Chem. 43 (2019) 5020–5031.
[17] (a) C.Y. Huang, S.G. Rhee, P.B. Chock, Annu. Rev. Biochem. 51 (1982) 935–971;
(b) E. Gallo, E. Solari, N. Re, C. Floriani, A. Chiesi-Villa, C. Rizzoli, J. Am. Chem. Soc. 119 (1997) 5144–5154;
(c) H. Miyasaka, N. Matsumoto, H. Okawa, N. Re, E. Gallo, C. Floriani, J. Am. Chem. Soc. 118 (1996) 981–994.
[18] (a) C. T. Lyons, T. D. P. Stack, Coord. Chem. Rev. 257 (2013) 528-540. (b) P. Seth, L. K. Das, M. G. B. Drew, A. Ghosh, Eur. J. Inorg. Chem. 2012 (2012) 2232-2242. (c) M. Mitra, T. Kundu, G. Kaur, G. Sharma, A. R. Choudhury, Y. Singh, R. Ghosh, RSC Adv. 2016 (6) 58831-58838.
[19] (a) S.K. Dey, A. Mukherjee, Coord. Chem. Rev. 310 (2016) 80–115;
(b) M. Shyamal, A. Saha, T.K. Mandal, Dalton Trans. 43 (2014) 5443–5452;
(e) C. Mukherjee, T. Weyhermueller, E. Bothe, E. Rentschler, P. Chaudhuri, Inorg. Chem. 46 (2007) 9895–9905.
[20] Z.L. He, X.E. Yang, P.J. Stoffella, J Trace Elem Med Biol. 19 (2005) 125–140.
[21] M. Hamatake, K. Iguchi, K. Hirano, R. Ishida, J Biochem. 128 (2000) 933–939.
[22] C. DeSantis, J. Ma, L. Bryan, A. Jemal, CA Cancer J. Clin. 64 (2014) 52–62.
[23] (a) R.A. Alderden, M.D. Hall, T.W. Hambley, J. Chem. Ed. 83 (2006) 728–735;
(b) R. Huang, A. Wallquist, D.G. Covell, Biochem. Pharmacol. 69 (2005) 1009–1039;
(c) B. Lippert, Cisplatin: Chemistry and Biochemistry of a Leading Anticancer Drug, Wiley-VCH, Zurich, 1999;
(d) C.S. Allardyce, P.J. Dyson, Platinum Met. Rev. 45 (2001) 62–69.
[24] (a) J. L. Biedler L. Helson, Cancer Res. 33 (11) (1973) 2643–52. (b) J. L. Biedler, S. Roffler-Tarlov, M. Schachner, L. S. Freedman, Cancer Res. 38 (11) (1978) 3751–7. (c) J. I. Johnsen, C. Dyber, M. Wickström, Front. Mol. Neuroscience. 12 (2019) 9. (d) G. M. Brodeur Cell and tissue research. 372(2) (2018) 277-86.
[25] A. Hazari, L.K. Das, A. Bauza, A. Frontera, A. Ghosh, Dalton Trans. 43 (2014) 8007–8015.
[26] D.L. Reger, T.D. Wright, C.A. Little, J.J.S. Lamba, M.D. Smith, Inorg. Chem. 40 (2001) 3810–3814.
[27] H. Fleischer, D. Schollmeyer, Inorg. Chem. 43 (2004) 5529–5536.
[28] A. Morsali, A.R. Mahjoub, Helv. Chim. Acta. 87 (2004) 2717–2722.
[29] J. Parr, Polyhedron 16 (1997) 551–566. [30] A. Olvera, G. Shi, H. Djieutedjeu, A. Page, C. Uher, E. Kioupakis, P. F. P. Poudeu, Inorg. Chem. 54 (2015) 746–755.
[30] C.A. Randall, A.S. Bhalla, T.R. Shrout, L.E. Cross, J. Mater. Res. 5 (1990) 829–834.
[31] F. Cheng, J. Liang, Z. Tao, J. Chen, Adv. Mater. 23 (2011) 1695–1715.
[32] L. Zhang, Y.-Y. Qin, Z.-J. Li, Q.-P. Lin, J.-K. Cheng, J. Zhang, Y.-G. Yao, Inorg. Chem. 47 (2008) 8286–8293.
[33] Y. Cheng, T.J. Emge, J.G. Brennan, Inorg. Chem. 35 (1996) 342–346.
[34] (a) G. Mahmoudi, A. Bauzá, A. Frontera, Dalton Trans. 45 (2016) 4965–4969. (b) M. S. Gargari, V. Stilinović, A. Bauzá, A. Frontera, P. McArdle, D. V. Derveer, S. W. Ng, G. Mahmoudi, Chem. – Eur. J. 21 (2015) 17951–17958.
[35] K.S. Pitzer, Relativistic Effects on Chemical Properties, Acc. Chem. Res. 12 (1979) 271–276.
[36] P. Pyykkö, J. -P. Desclaux, Relativity and the periodic system of elements, Acc. Chem. Res. 12 (1979) 276–281.
[37] P. Pyykkö, Relativistic Effects in Structural Chemistry, Chem. Rev. 88 (1988) 563–594.
[38] N.V. Sidgwick, H.M. Powell, Bakerian Lecture: Stereochemical types and valency groups, Proc. R. Soc. (London) A 176 (1940) 153.
[39] J.R. Thompson, D. Snider, J.E.C. Wren, S. Kroeker, V.E. Williams, D.B. Lenzoff, Eur. J. Inorg. Chem. (2017) 88–98.
[40] R.L. Davidovich, V. Stavila, D.V. Marinin, E.I. Voit, K.H. Whitmire, Coord. Chem. Rev. 253 (2009) 1316–1352.
[41] R.J. Gillespie, R.S. Nyholm, Inorganic Stereochemistry, Q. Rev., Chem. Soc. 11 (1957) 339–380.
[42] (a) D.J. Majumdar, S. Dey, A. Kumari, T.K. Pal, K. Bankura, D. Mishra, Spectrochim Acta. Part A 254 (2021), 119612;
(b) L.E. Orgel, Spectra of Transition-metal Complexes, J. Chem. Phys. 23 (1955) 1004–1014.
[43] (a) G.L. Miessler, D.A. Tarr, Inorg, Chem. Pearson Education, Upper Saddle River, N, J. (2004) 345;
(b) , 4th edn,, Freeman and Company, New York, 2006, p. 459;
(c) K.L. Haas, K.J. Franz, Chem. Rev. 109 (2009) 4921–4960.
[44] W.N. Lipscomb, N. Strater, Chem. Rev. 96 (1996) 2375–2433.
[45] I. Bertini, H.B. Gray, S.J. Lippard, J.S. Valentine, Bioinorganic Chemistry, University Science Books, Mill Valley, CA, 1994.
[46] (a) M.P. Heng, K.S. Sim, K.W. Tan, J. Inorg. Biochem. 208 (2020), 111097;
(b) R. Fujishiro, H. Sonoyama, Y. Ide, T. Fujimura, R. Sasai, A. Nagai, S. Mori, N.E. M. Kaufman, Z. Zhou, M.G.H. Vicente, T. Ikeue, J. Inorg. Biochem. 192 (2019) 7–16;

(c) M. Saswati, A. Mohanty, S. Banerjee, A. Horn Biswal, G. Jr, K. Schenk, E. Brzezinski, H. Sinn, R. Dinda Reuter, J. Inorg. Biochem. 203 (2020), 110908;
(d) C.P. Matos, Y. Addis, P. Nunes, S. Barroso, I. Alho, M. Martins, A.P.A. Matos, F. Marques, I. Cavaco, J. Costa Pessoa, I. Correia, J. Inorg. Biochem. 198 (2019), 110727;
(e) Z.-M. Yu, X.-M. Wan, M. Xiao, C. Zheng, X.-L. Zhou, J. Inorg. Biochem. 217 (2021), 111389;
(f) J. Li, R. Liu, J. Jiang, X. Liang, G. Huang, D. Yang, H. Chen, L. Pan, Z. Ma, J. Inorg. Biochem. 210 (2020), 111165.

[47] D.J. Majumdar, Y. Agrawal, R. Thomas, Z. Ullah, M.K. Santra, S. Das, T.K. Pal, K. Bankura, D. Mishra, Appl. Organomet. Chem. 34 (2020), e5269.

[48] (a) D.J. Majumdar, S. Das, R. Thomas, Z. Ullah, S.S. Sreejith, S. Das, P. Shukla, K. Bankura, D. Mishra, Inorg. Chim. Acta. 492 (2019) 221–234;
(b) D.J. Majumdar, J.E. Philip, S. Das, B.K. Kundu, R.V. Saini, G. Chandan, K. Bankura, D. Mishra, J. Mol. Struct. 1225 (2020), 129189.

[49] (a) D.J. Majumdar, T.K. Pal, D.K. Singh, D.K. Pandey, D. Parai, K. Bankura, D. Mishra, J. Mol. Struct. 1209 (2020), 127936;
(b) S. Wu, L. Qi, Y. Ren, H. Ma, J. Mol. Struct. 1219 (2020), 128591;
(c) D.J. Majumdar, T.K. Pal, S.A. Sakib, S. Das, K. Bankura, D. Mishra, Inorg. Chem. Commun. 128 (2021), 108609.

[50] M. J. Frisch, G. W. Trucks, H. B. Schlegel, G. E. Scuseria, M. A. Robb, J. R. Cheeseman, G. Scalmani, V. Barone, G. A. Petersson, H. Nakatsuji, X. Li, M. Caricato, A. V. Marenich, J. Bloino, B. G. Janesko, R. Gomperts, B. Mennucci, H. P. Hratchian, J. V. Ortiz, A. F. Izmaylov, J. L. Sonnenberg, D. Williams-Young, F. Ding, F. Lipparini, F. Egidi, J. Goings, B. Peng, A. Petrone, T. Henderson, D. Ranasinghe, V. G. Zakrzewski, J. Gao, N. Rega, G. Zheng, W. Liang, M. Hada, M. Ehara, K. Toyota, R. Fukuda, J. Hasegawa, M. Ishida, T. Nakajima, Y. Honda, O. Kitao, H. Nakai, T. Vreven, K. Throssell, J. A. Montgomery, Jr., J. E. Peralta, F. Ogliaro, M. J. Bearpark, J. J. Heyd, E. N. Brothers, K. N. Kudin, V. N. Staroverov, T. A. Keith, R. Kobayashi, J. Normand, K. Raghavachari, A. P. Rendell, J. C. Burant, S. S. Iyengar, J. Tomasi, M. Cossi, J. M. Millam, M. Klene, C. Adamo, R. Cammi, J. W. Ochterski, R. L. Martin, K. Morokuma, O. Farkas, J. B. Foresman, J. V. Ortiz, J. Cioslowski, D. J. Fox, Gaussian 09, revision D.01. Gaussian Inc, Wallingford CT, 2009.

[51] D. W. Ritchie, V. Venkatraman, Bioinformatics (Oxford, England), 26(19) (2010) 2398–2405.

[52] (a) W.L. DeLano, CCP4 Newsletter on Protein Crystallography 40 (2002) 82–92;
(b) R. Sharma, G. Chandan, A. Chahal, R.V. Saini, Int. J. Pharm Pharm Sci. 9 (2) (2017) 245–249;
(c) G. Chandan, C. Kumar, M.K. Verma, N.K. Satti, A.K. Saini, R.V. Saini, 3, Biotech. 10 (10) (2020) 1–14;
(d) A. Baracca, G. Sgarbi, G. Solaini, G. Lenaz, Biochem. Biophys Acta. 1606 (2003) 137–146.

[53] G. M. Sheldrick, SADABS, a software for empirical absorption correction, Ver.2.05; University of Göttingen: Göttingen, Germany, 2002.

[54] SMART & SAINT Software Reference manuals Version 6.45; Bruker Analytical X-ray Systems, Inc.: Madison, WI, 2003.

[55] SHELXTL Reference Manual Ver. 6.1; Bruker Analytical X-ray Systems, Inc.: Madison, WI, 2000.

[56] G. M. Sheldrick, SHELXTL, a software for empirical absorption correction Ver.6.12; Bruker AXS Inc.: WI. Madison, 2001.

[57] O.V. Dolomanov, L.J. Bourhis, R.J. Gildea, J.A.K. Howard, H. Puschmann, OLEX2, *OLEX2*: a complete structure solution, refinement, and analysis program, J. Appl. Crystallog. 42 (2009) 339–341.

[58] I. Mondal, S. Chatterjee, S. Chattopadhyay, Polyhedron 190 (2020), 114735.

[59] (a) S. Dey, S. Sil, B. Dutta, K. Naskar, S. Maity, P.P. Ray, C. Sinha, ACS Omega 22 (4) (2019) 19959–19968;
(b) S. Mirdya, S. Roy, S. Chatterjee, A. Bauza, A. Frontera, S. Chattopadhyay, Cryst. Growth Des. 19 (2019) 5869–5881;
(c) S. Mirdya, A. Frontera, S. Chattopadhyay, CrystEngComm 21 (2019) 6859–6868.

[60] M. Maiti, S. Thakurta, D. Sadhukhan, G. Pilet, G.M. Rosair, A. Nonat, L. J. Charbonniere, S. Mitra, Polyhedron 65 (2013) 6–15.

[61] A.B.P. Lever, Inorganic Spectroscopy, second ed., Elsevier, New York, 1984.

[62] L.K. Das, M.G.B. Drew, A. Ghosh, Inorg. Chim. Acta. 394 (2013) 247–254.

[63] (a) J. Solé, L. Bausa, D. Jaque, An Introduction to the Optical Spectroscopy of Inorganic Solids, John Wiley & Sons, 2005;
(b) D.K. Mishra, U.K. Singha, A. Das, S. Dutta, P. Kar, A. Chakraborty, A. Sen, B. Sinha, J. Coord. Chem. 71 (2018) 2165–2182.

[64] (a) D. Sadhukhan, A. Ray, G. Rosair, L. Charbonnière, S. Mitra, BCSJ 84 (2011) 211–217;
(b) S. Hingorani, B.V. Agarwala, V. Puri, Met. Chem. 18 (1993) 576–578;
(c) S. Dehghanpour, A.H. Mahmoudkhani, M. Amirnasr, Struct. Chem. 17 (2006) 255–262;
(d) M. Amirnasr, K.J. Schenk, M. Salavati, S. Dehghanpour, A. Taeb, A. Tadjarodi, J. Coord. Chem. 56 (2003) 231–243.

[65] S. Roy, M.G.B. Drew, A. Bauza, A. Frontera, S. Chattopadhyay, New J. Chem. 42 (2018) 6062–6076.

[66] S. Ghosh, P. Chopra, S. Wategaonkar, Phys. Chem. Chem. Phys. 22 (2020) 17482–17493.

[67] L. Shimoni-Livny, J.P. Glusker, C.W. Bock, Inorg. Chem. 37 (1998) 1853–1867.

[68] M.-L. Hu, A. Morsali, L. Aboutorabi, Coord. Chem. Rev. 255 (2011) 2821–2859.

[69] R.G. Pearson, J. Am. Chem. Soc. 85 (22) (1963) 3533–3539.

[70] A.W. Addison, T.N. Rao, J. Reedijk, J.V. Rijn, G.C. Verschoor, J. Chem. Soc. Dalton Trans. (1984) 1349–1356.

[71] K. Sayin, J. Coord. Chem. 71 (20) (2018) 3292–3303.

[72] (a) Ü.M. Koçyiğit, P. Taslimi, B. Tüzün, H. Yakan, H. Muğlu, E. Güzel, J. Biomol. Struct. Dyn. 49 (2020) 1–11.(b)A. Aktas, B. Tuzun, R. Aslan, K. Sayin, H. Ataseven, J. Biomol. Struct. Dyn. (2020) 1-11/https://doi.org/10.1080/07391102.2020.1806112.

[73] M. Sheng, Y. Zhao, A. Zhang, L. Wang, G. Zhang, J. Pept. Sci. 20 (2014) 803–810.

[74] (a) M.R. Shah, C.L. Kriedt, N.H. Lents, M.K. Hoyer, N. Jamaluddin, C. Klein, J. Baldassare, J. Exp. Clin. Cancer Res. 28 (1) (2009) 1–10;
(b) P.S. Lecane, M.W. Karaman, M. Sirisawad, L. Naumovski, R.A. Miller, J. G. Hacia, D. Magda, Cancer Res. 65 (24) (2005) 11676–11688.

[75] S. Swaminathan, J. Haribabu, N. K. Kalagatur, R. Konakanchi, N. Balakrishnan, Nattamai Bhuvanesh, R. Karvembu, ACS Omega 4 (2019) 6245-6256.

[76] D. Trachootam, J. Alexandre, P. Huang, Nat. Rev. Drug Discov. 8 (2009) 579–591.

[77] G.S. Salvesen, V.M. Dixit, Cell. 91 (1997) 443–446.

[78] R. Kumari, A.K. Saini, A. Kumar, R.V. Saini, J. Biol. Inorg. Chem. 25 (1) (2020) 223–237.